Utilising Acoustic Techniques to Improve Understanding of the Formation Process in Sodium-ion Batteries

Arthur Fordham[1,3,6,=], Dylan Wee[2,3,=], Rhodri Owen[3,7], Tongjun Luo[4,6], Roksana Jackowska[3,5], Tianqi Jia[4], Yan Zheng[4], Emma Kendrick [3,5], Wesley M. Dose[4,6], Dan J. L. Brett[8], Paul R. Shearing[3,9] James Robinson[1,3,7,*], Rhodri Jervis[1,3,7*]

[1] Electrochemical Innovation Lab, Department of Chemical Engineering, University College London, London, WC1E 7JE, UK

[2] Department of Mechanical Engineering, Imperial College London, London, SW7 2BX, UK

[3]The Faraday Institution, Quad One, Harwell Science and Innovation Campus, Didcot, UK, OX11 0RA, UK

[4]School of Chemistry, University of Sydney, Camperdown, NSW 2006, Australia.

[5] School of Metallurgy and Materials, University of Birmingham, Birmingham, B15 2SE, UK

[6]School of Chemistry, University of New South Wales, Sydney, NSW 2052, Australia

[7]Advanced Propulsion Lab, Marshgate, 7 Sidings Street, University College London, London, E20 2AE, UK

[8]Prosemino, Unit 2, Paper Yard, Quebec Way, London SE16 7LG

[9]ZERO Institute, Holywell House, Osney Mead, University of Oxford, Oxford, OX2 0ES, UK

*Corresponding authors: j.b.robinson@ucl.ac.uk, rhodri.jervis@ucl.ac.uk

Supplementary Information

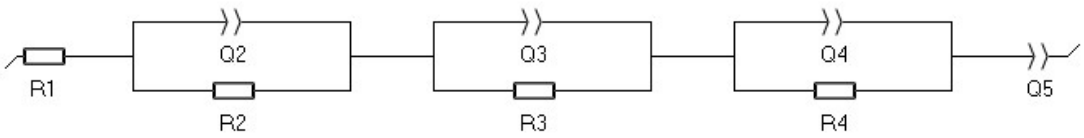

Figure S 1. Equivalent Circuit Model used to fit the Potentiostatic Electrochemical Impedance Spectroscopy (PEIS).

Table 1. Fitted Resistance Values for the EIS using the Equivalent Circuit Model (ECM) outlined above.

Fitted Resistance Values

Additive	Voltage (V)	Cycle Number (n)	R_2 (Ω)	R_3 (Ω)	R_4 (Ω)	R_total (Ω)
FEC	2.9	0	0.3767	0.3341	0.9696	1.6804
FEC	2.9	50	0.1646	0.4448	0.9411	1.5506
FEC	2.9	100	0.4001	0.3527	0.8942	1.647
FEC	2.9	150	0.4329	0.3459	0.939	1.7178
FEC	2.9	200	0.3786	0.3548	1.0328	1.7662
FEC	2.9	250	0.5122	0.2827	1.0462	1.8411
FEC	2.9	300	0.509	0.2707	1.1153	1.8951
FEC	2.9	350	0.3915	0.3466	1.2106	1.9487
FEC	2.9	400	0.3635	0.3538	1.2456	1.9629
FEC	2.9	450	0.3407	0.3933	1.3076	2.0415
FEC	3.3	0	0.52	0.332	0.6548	1.5068
FEC	3.3	50	0.4239	0.1394	0.6549	1.2182
FEC	3.3	100	0.4417	0.1258	0.5948	1.1623
FEC	3.3	200	0.3374	0.3777	0.4994	1.2145
FEC	3.3	250	0.4012	0.2224	0.6052	1.2288
FEC	3.3	250	0.4186	0.3523	0.4679	1.2388
FEC	3.3	300	0.4455	0.3486	0.4783	1.2723
FEC	3.3	350	0.4423	0.3601	0.4779	1.2803
FEC	3.3	400	0.44	0.3654	0.5204	1.3257
FEC	3.3	450	0.4749	0.3807	0.4922	1.3479
FEC	3.7	0	0.518	0.3339	0.5878	1.4397
FEC	3.7	50	0.3254	0.3362	0.3934	1.055
FEC	3.7	100	0.3596	0.3298	0.3625	1.0519
FEC	3.7	150	0.3687	0.3229	0.3834	1.075
FEC	3.7	200	0.3834	0.323	0.3881	1.0945
FEC	3.7	250	0.3876	0.3497	0.3757	1.1131
FEC	3.7	300	0.377	0.3545	0.395	1.1265
FEC	3.7	350	0.3646	0.3601	0.4111	1.1358
FEC	3.7	400	0.3956	0.357	0.394	1.1467
FEC	3.7	450	0.3919	0.3607	0.4046	1.1572
FEC + VC	2.9	0	1.3554	0.0882	1.3035	2.7471

FEC + VC	2.9	50	1.8564	0.1141	1.7381	3.7085
FEC + VC	2.9	100	2.0682	0.1102	1.9575	4.1358
FEC + VC	2.9	150	1.9498	0.1066	2.4524	4.5088
FEC + VC	2.9	200	1.8344	0.1051	2.7631	4.7026
FEC + VC	2.9	250	1.8651	0.1035	2.9673	4.9358
FEC + VC	2.9	300	1.7877	0.105	3.2063	5.0989
FEC + VC	2.9	350	1.8091	0.1022	3.3516	5.263
FEC + VC	2.9	400	1.797	0.1038	3.5029	5.4038
FEC + VC	2.9	450	1.8172	0.1011	3.5945	5.5128
FEC + VC	3.3	0	0.7625	0.9939	1.2228	2.9792
FEC + VC	3.3	50	0.6376	0.9851	0.9875	2.6102
FEC + VC	3.3	100	0.7427	0.9692	1.0264	2.7383
FEC + VC	3.3	150	0.7513	0.9987	1.1496	2.8996
FEC + VC	3.3	200	0.6145	0.9972	1.2879	2.8997
FEC + VC	3.3	250	0.1241	1.0006	1.6602	2.7848
FEC + VC	3.3	300	0.1153	0.9988	1.7517	2.8658
FEC + VC	3.3	350	0.107	0.9987	1.8792	2.9849
FEC + VC	3.3	400	0.1114	0.9981	1.9156	3.0251
FEC + VC	3.3	450	0.1062	0.9985	2.0117	3.1163
FEC + VC	3.7	0	0.0634	1.2355	1.1461	2.4451
FEC + VC	3.7	50	0.1261	0.9079	1.0038	2.0378
FEC + VC	3.7	100	0.1323	0.9226	0.9712	2.0261
FEC + VC	3.7	150	0.1275	0.9479	0.9608	2.0362
FEC + VC	3.7	200	0.1246	0.9669	0.9716	2.063
FEC + VC	3.7	250	0.1293	1.0432	0.9154	2.0879
FEC + VC	3.7	300	0.1257	1.0735	0.9224	2.1216
FEC + VC	3.7	350	0.1212	1.0888	0.951	2.161
FEC + VC	3.7	400	0.125	1.0992	0.9611	2.1853
FEC + VC	3.7	450	0.1222	1.1214	0.9718	2.2153
No Additive	2.9	0	0.17	0.2171	0.258	0.6451
No Additive	2.9	50	0.4328	0.8377	0.928	2.1985
No Additive	2.9	100	0.504	0.931	0.9519	2.3869
No Additive	2.9	150	0.5533	0.9921	1.165	2.7104
No Additive	2.9	200	0.5693	1.02	1.183	2.7723
No Additive	2.9	250	0.595	1.132	1.258	2.985
No Additive	2.9	300	0.612	1.216	1.305	3.133
No Additive	2.9	350	0.652	1.36	1.477	3.489
No Additive	2.9	400	0.688	1.412	1.556	3.656
No Additive	2.9	450	0.692	1.467	1.592	3.751
No Additive	3.3	0	0.13	0.1141	0.177	0.4211
No Additive	3.3	50	0.2925	0.6529	0.5921	1.5375
No Additive	3.3	100	0.3237	0.7097	0.6751	1.7085
No Additive	3.3	150	0.4596	0.747	0.713	1.9196
No Additive	3.3	200	0.4819	0.792	0.784	2.0579
No Additive	3.3	250	0.547	0.878	0.864	2.289
No Additive	3.3	300	0.585	0.896	0.881	2.362

No Additive	3.3	350	0.6339	0.915	0.958	2.5069
No Additive	3.3	400	0.68	0.951	0.977	2.608
No Additive	3.3	450	0.694	0.971	0.991	2.656
No Additive	3.7	0	0.12	0.1291	0.139	0.3881
No Additive	3.7	50	0.2934	0.474	0.514	1.2814
No Additive	3.7	100	0.3779	0.5597	0.584	1.5216
No Additive	3.7	150	0.406	0.571	0.614	1.591
No Additive	3.7	200	0.4271	0.6064	0.6655	1.699
No Additive	3.7	250	0.467	0.6818	0.7678	1.9166
No Additive	3.7	300	0.496	0.705	0.7915	1.9925
No Additive	3.7	350	0.515	0.716	0.8061	2.0371
No Additive	3.7	400	0.541	0.754	0.841	2.136
No Additive	3.7	450	0.551	0.563	0.851	1.965

Synchrotron X-ray Diffraction of Electrodes

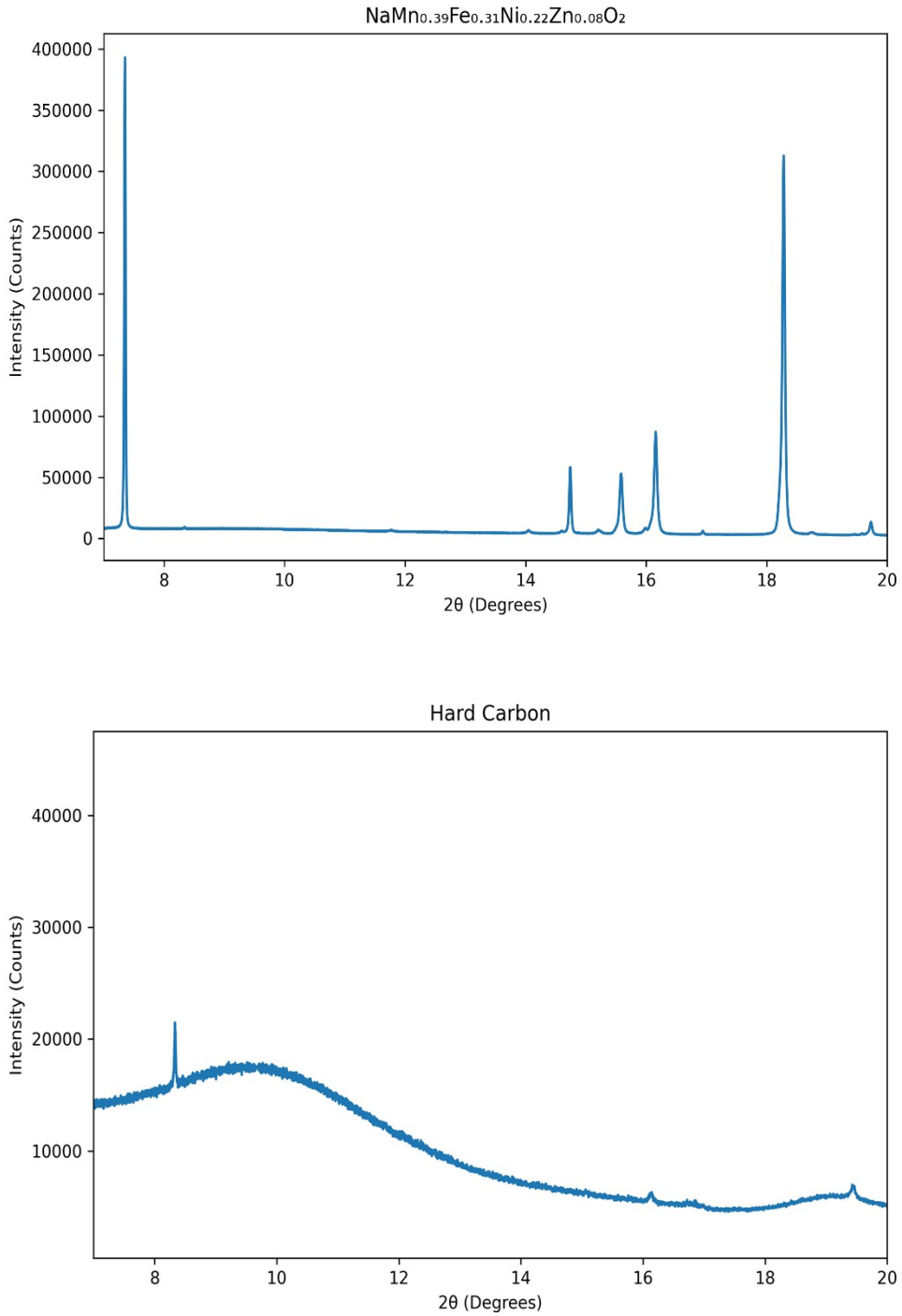

Figure S 2. Synchrotron X-ray Diffraction patterns of the respective electrodes.

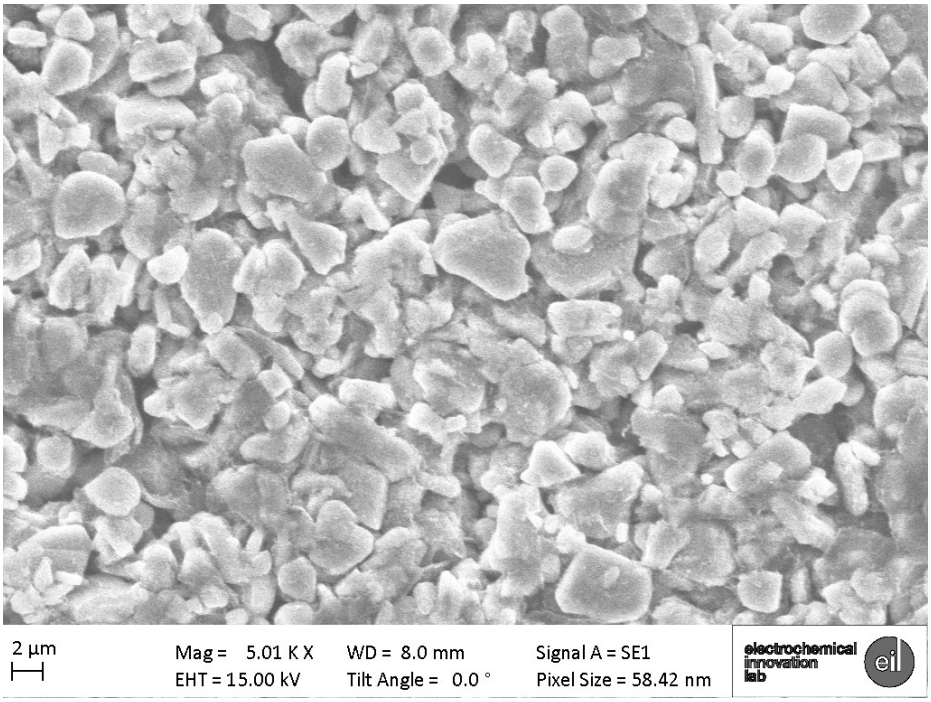

Figure S 4. Scanning Electron Microscopy of the positive electrode $NaMn_{0.39}Fe_{0.31}Ni_{0.22}Zn_{0.08}O_2$, revealing densely packed secondary particles with an average particle size in the range of 0.5–5 µm. The particles exhibit irregular, angular morphologies with relatively uniform distribution, indicating a well-synthesized layered oxide structure suitable for sodium-ion intercalation. The compact surface texture and interparticle contact suggest good electronic percolation within the electrode.

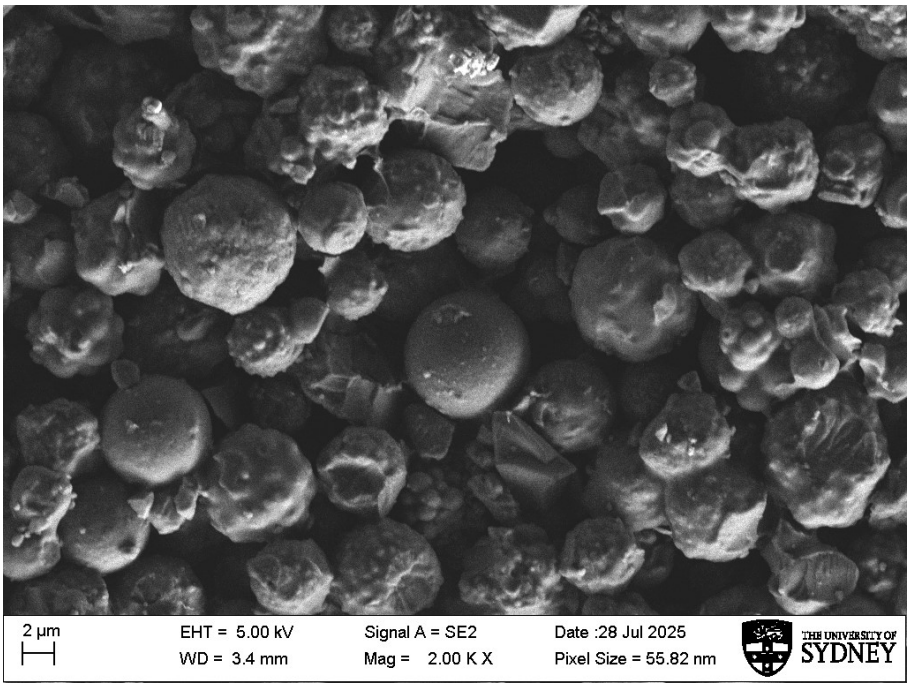

Figure S 3. Scanning Electron Microscopy of the hard carbon sample, displaying aggregated spherical and sub-spherical particles with diameters in the range of ~0.5–3 µm. The particles exhibit a rough, porous surface texture and irregular morphologies characteristic of non-graphitizable carbon. The densely packed structure with visible interparticle voids suggests a disordered microstructure conducive to sodium-ion storage via pore filling and adsorption mechanisms.

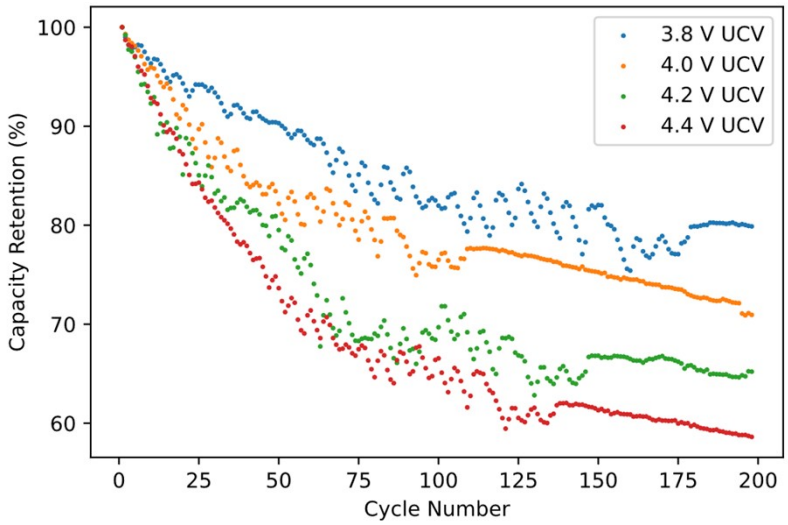

Figure S 6. Comparison of capacity retention vs. cycle number at different upper cutoff voltages (UCVs) of 3.8 V, 4.0 V, 4.2 V, and 4.4 V. The results demonstrate the rationale for selecting 3.8 V in our experiments for optimal capacity retention. Fluctuations in the data are due to slight variations in the room temperature.

Effect of Cycling Upper-Cut off Voltage

Since there is limited research on sodium-ion formation cycles, studies were conducted to identify the optimal upper cut-off voltage (UCV) for the Na-ion cells used in this work. Using an electrolyte composed of 1 M $NaPF_6$ in 1:1 EC:DMC with 5% FEC, cells were formed under consistent conditions within a voltage window, recommended by cell manufacturers, of 1.5 V to 4.0 V for the initial two cycles at a C-rate of C/20. After formation, the cells were cycled for 200 cycles, each with a different UCV (3.8 V, 4.0 V, 4.2 V, and 4.4 V), to assess their long-term performance **Figure S *6***. The results showed that the cell cycled with a 3.8 V upper cut-off voltage (UCV) was the only one to retain 80% of its initial capacity after 200 cycles. This cell significantly outperformed those cycled at higher UCVs, which exhibited faster degradation and lower capacity retention. These findings indicate that voltages of 4 V and above are too high for this cathode, leading to the decision to limit the UCV to 3.8 V for all subsequent formation cycles and experiments aimed at optimising cell performance.

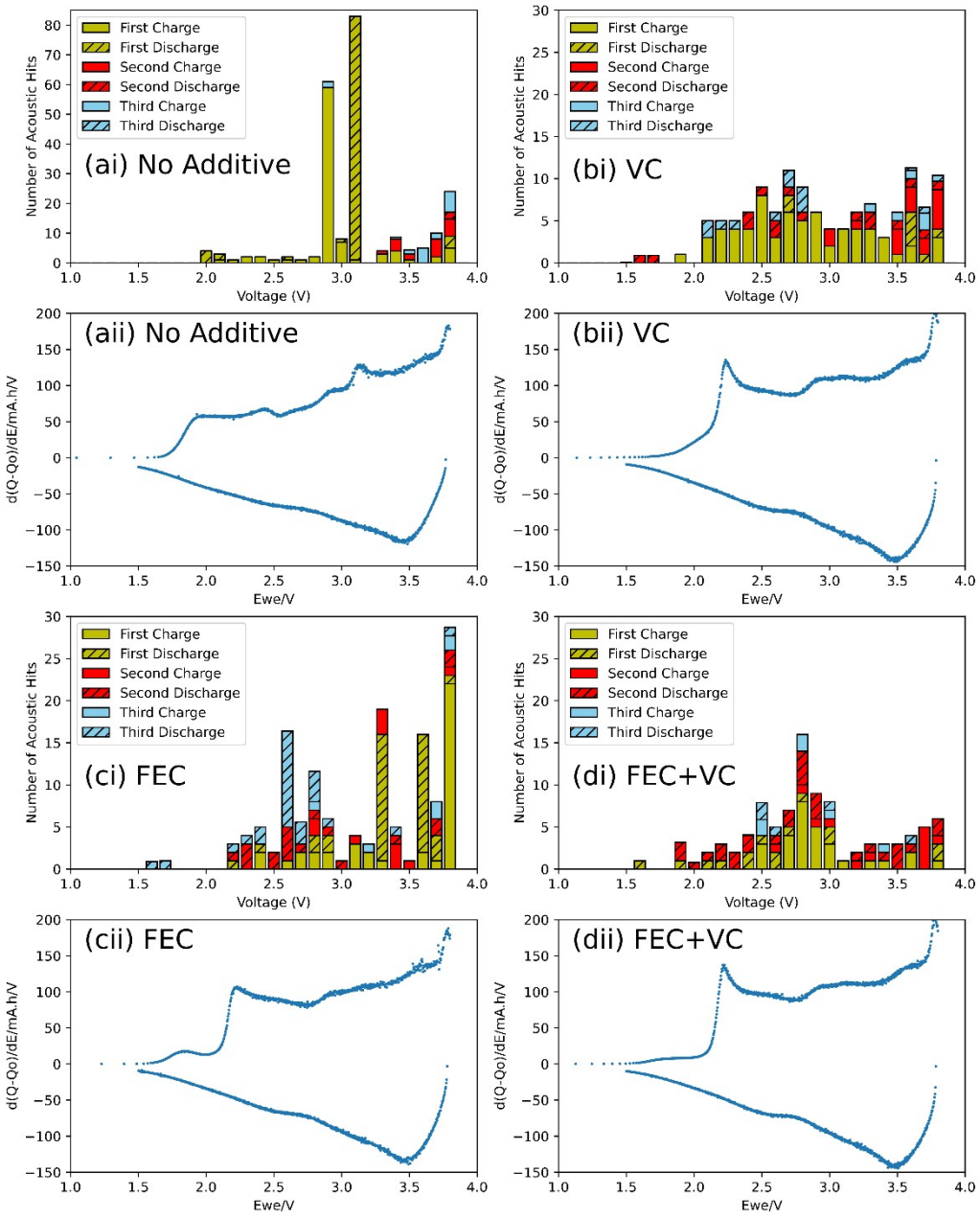

Figure S 7. AE histogram and dQ/dV plots. (ai, bi, ci, di) Number of AE hits for each charge/discharge process plotted against cell voltage in 0.1V divisions. (aii, bii, cii, dii): dQ/dV from the C/20 formation cycle plotted against cell voltage. (a) No Additive cell. (b) VC additive cell. (c) FEC additive cell. (d) VC and FEC additive cell for the first cycle. The dQ/dV data extracted from full-three electrode cell measurements using the same electrodes and electrolyte additives as the full pouch cells. The dQ/dV for both the charge and discharge of the formation cycle are displayed.

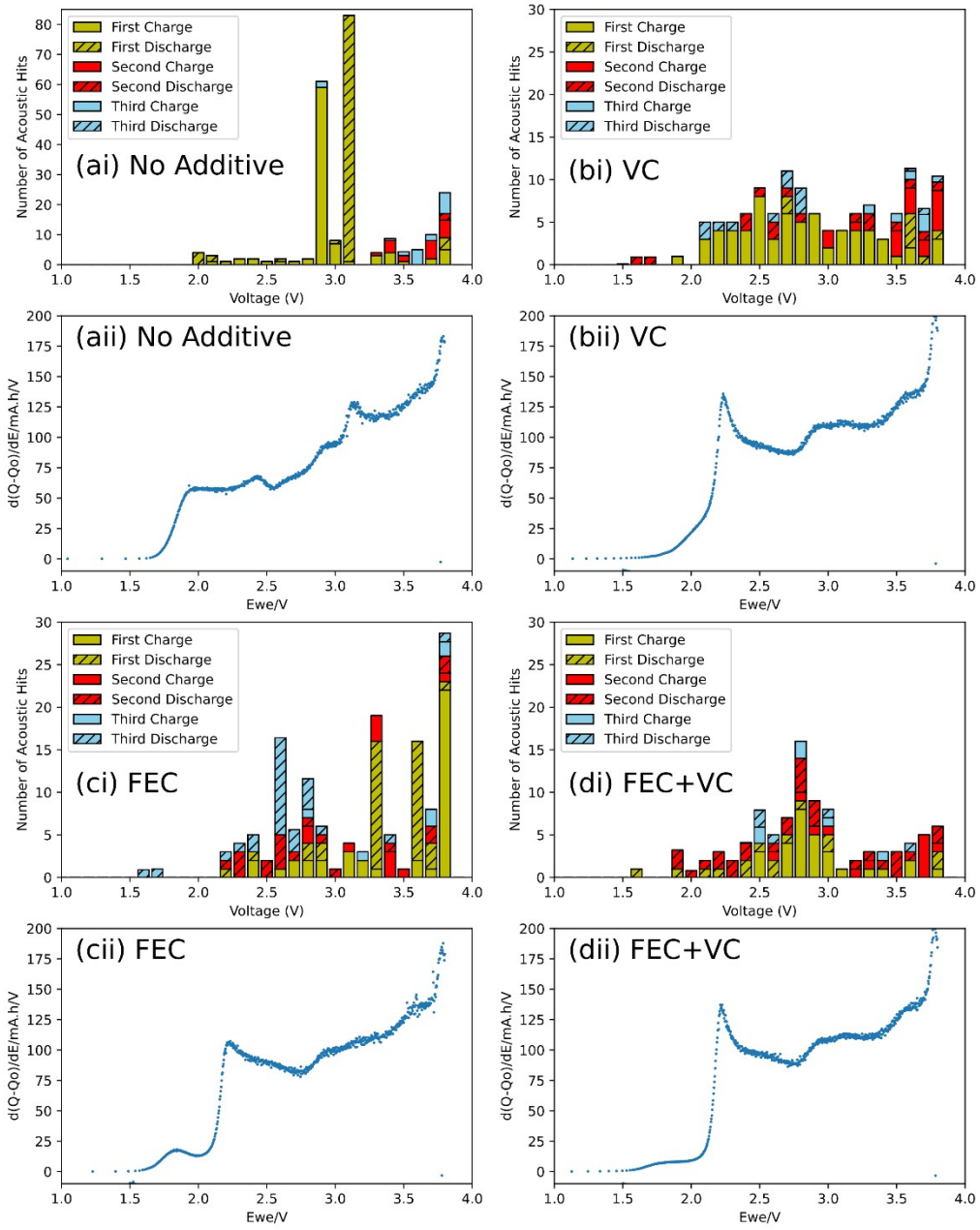

Figure S 8. Figure 3 but repeated with the dQ/dV data from the full 200 mAh pouch cells. AE histogram and dQ/dV plots. (ai, bi, ci, di) Number of AE hits for each charge/discharge process plotted against cell voltage in 0.1V divisions. (aii, bii, cii, dii): dQ/dV from the C/20 formation cycle plotted against cell voltage. (a) No Additive cell. (b) VC additive cell. (c) FEC additive cell. (d) VC and FEC additive cell for the first cycle The is dQ/dV data extracted from three electrode cell measurements using the same electrodes and electrolyte additives.

In the FEC cell, a peak appears at 1.7 V and a larger one at 2.2 V. This aligns with previous research, which attributed the 2.2 V feature to the reduction of FEC on the hard carbon negative electrode.[46] The smaller 1.7 V peak is likely due to EC reduction, and its reduced intensity compared to cells without

additives suggests that the FEC reduction involves greater charge transfer during SEI formation, overshadowing the contribution from EC. In the VC additive cell, there is a sharper, larger, peak at 2.3 V, attributed to VC reduction. FEC +VC additive cell observed a small peak at 1.7 V and then a sharp peak, very similar to the VC additive cell, at 2.3 V. The dQ/dV spectrum for the combined VC+FEC cell looks most like the VC dQ/dV spectrum, indicating that the VC additive controls the chemical behavior of SEI growth. [41]

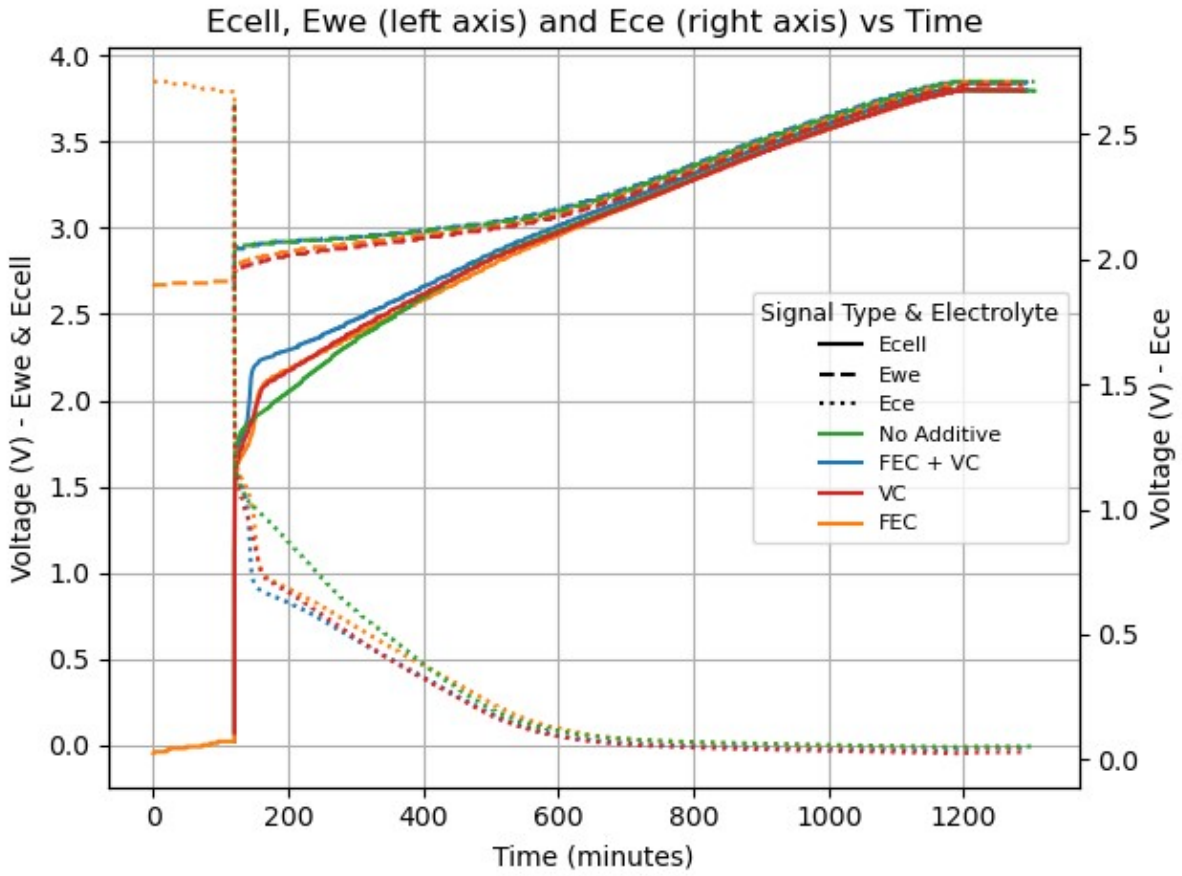

Figure S 9. Three - electrode data for voltage vs time during the first charge of formation.

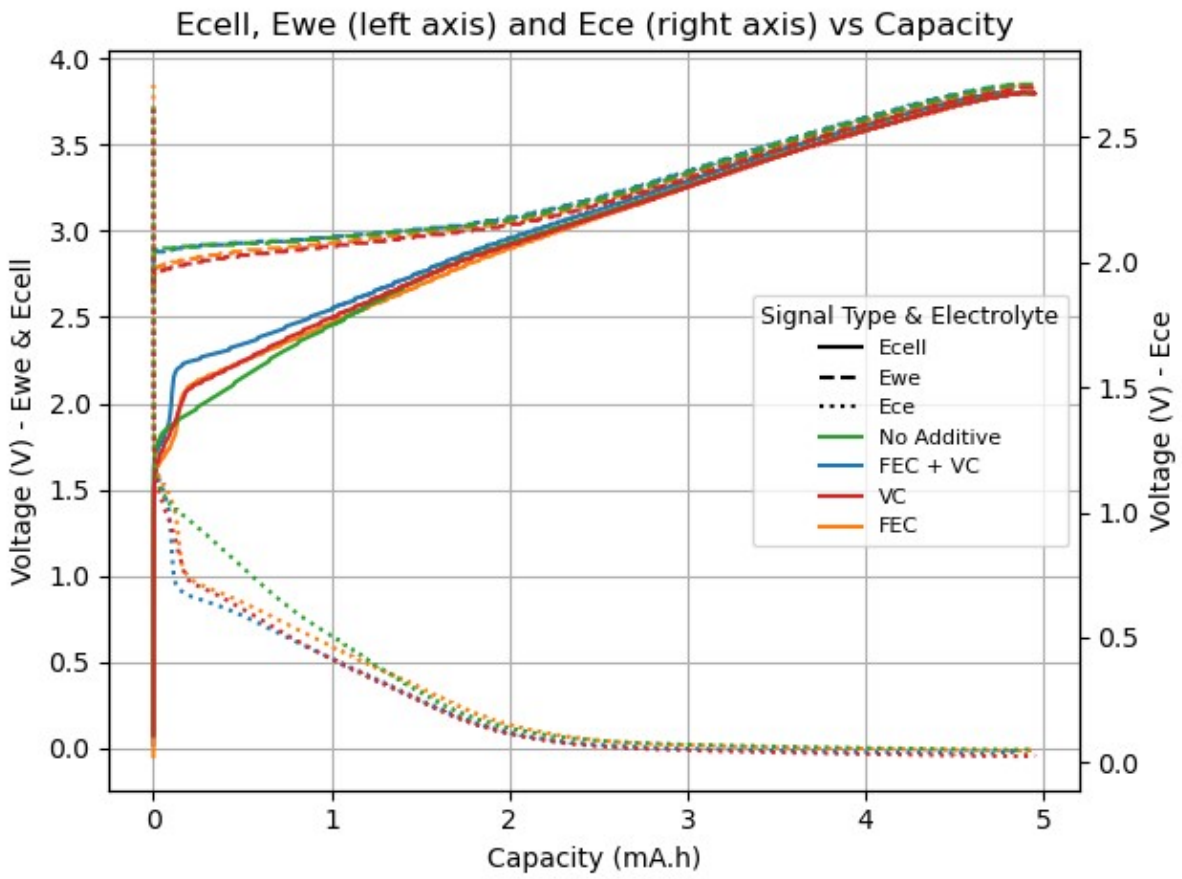

Figure S 10.Three - electrode data for voltage vs capacity during the first charge of formation.

Three electrode dQ/dV

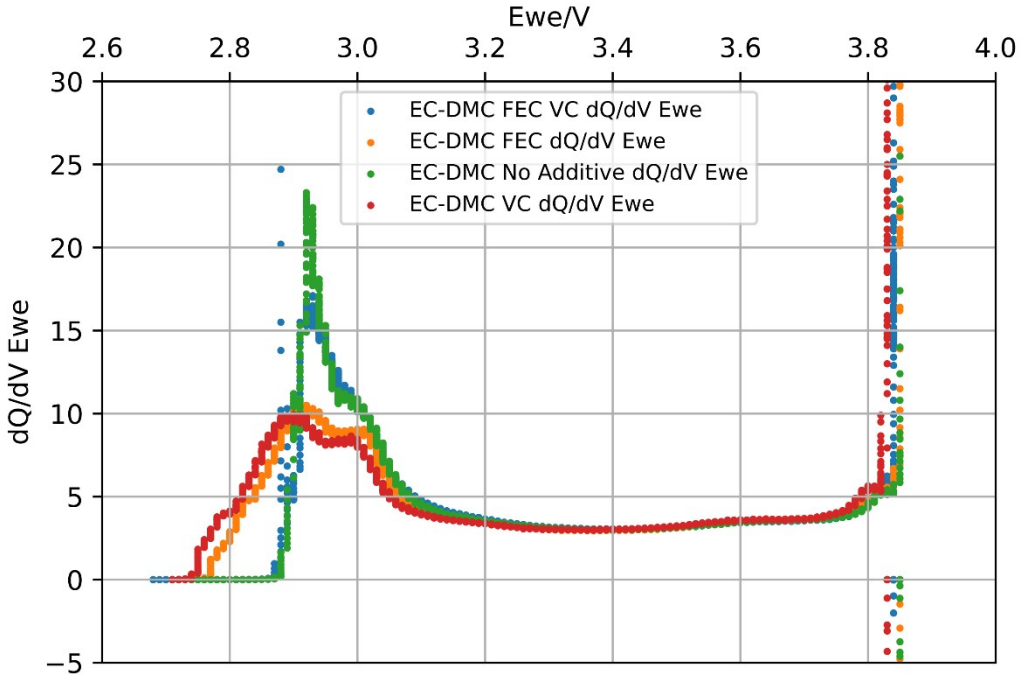

w

Figure S 11. Three - electrode data for dQ/dV of positive electrode during the first charge of formation.

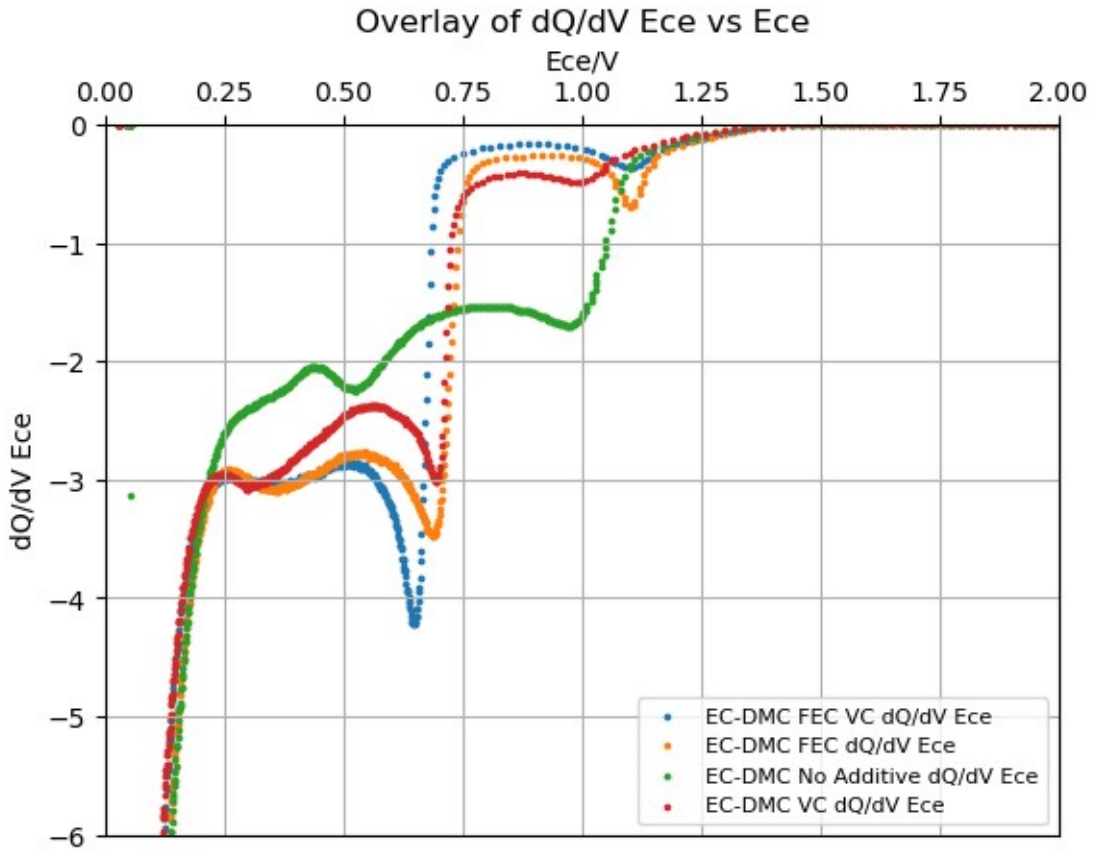

Figure S 12. Three - electrode data for dQ/dV of negative electrode during the first charge of formation.

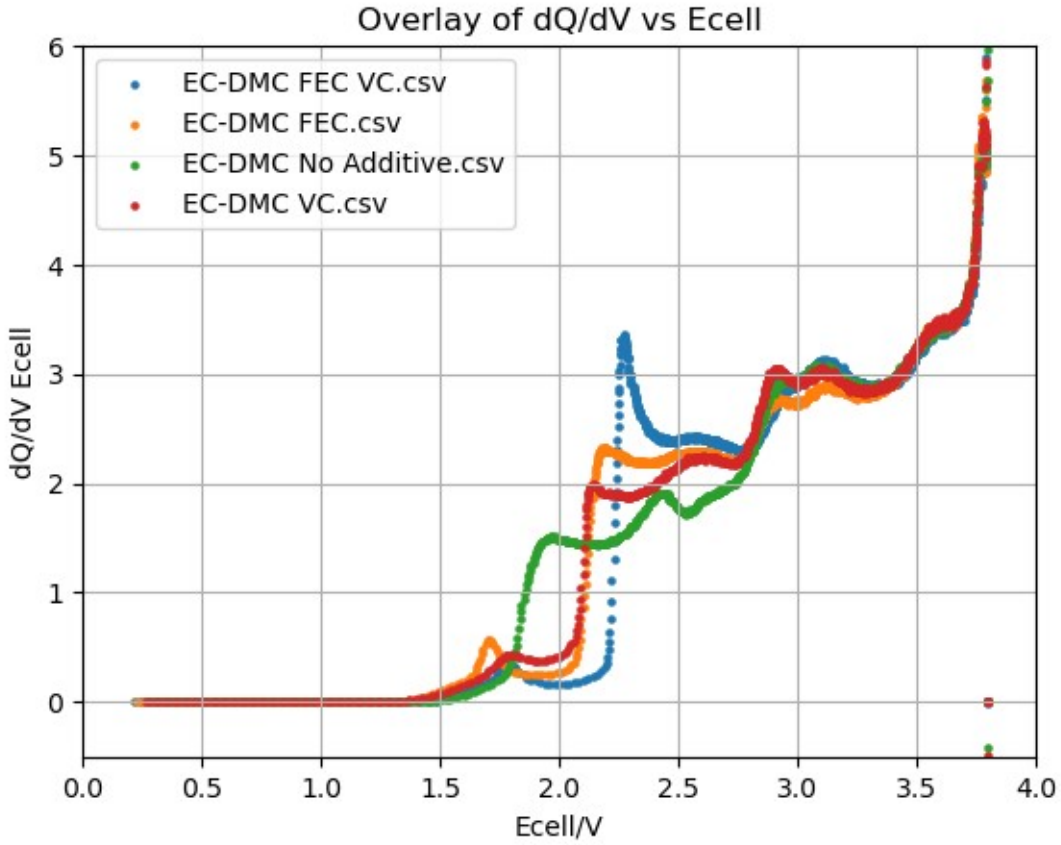

Figure S 13. Three - electrode data for dQ/dV of cell during the first charge of formation.

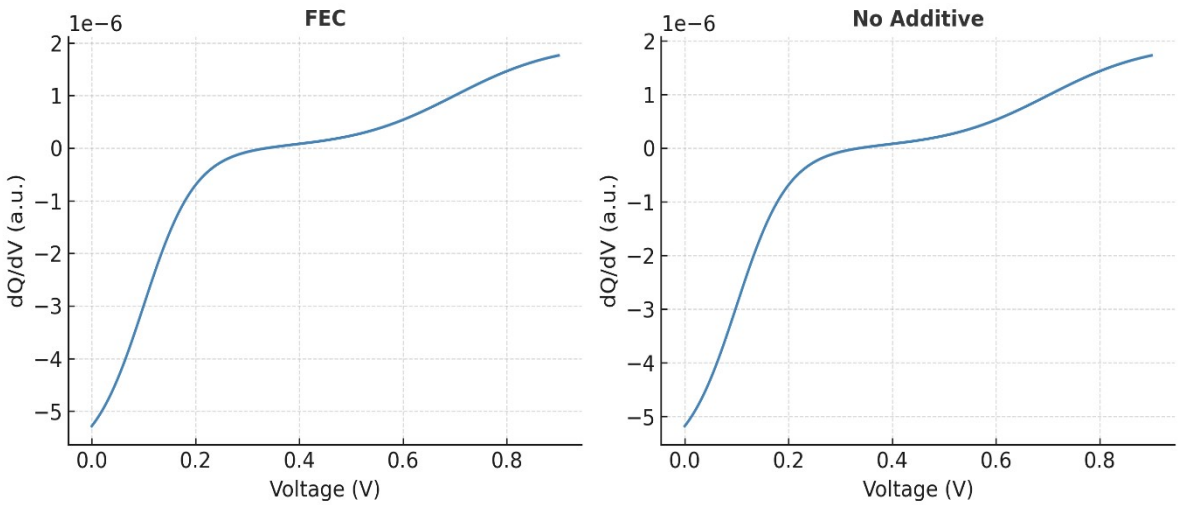

Figure S 14. Three - electrode data for dQ/dV of the negative electrode of the cell during the second and third formation cycles at C/3.

Repeats of Acoustics for Formation

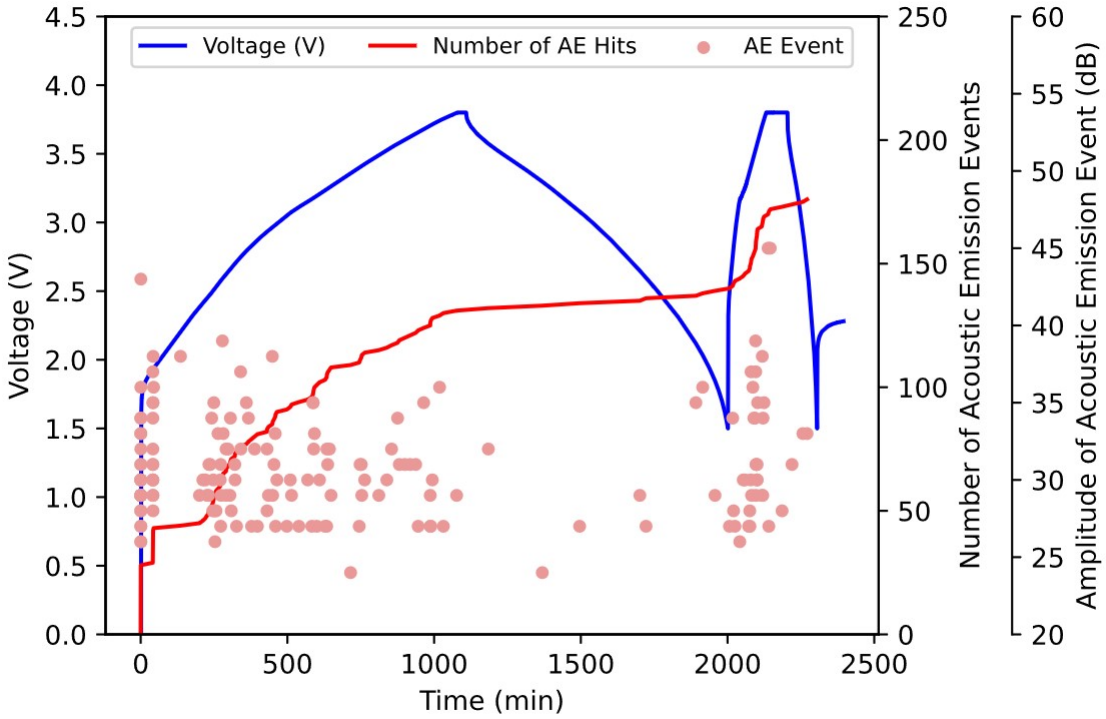

Figure S 15. Repeats of the Acoustic Emission data recorded during the formation cycle of cells containing different additices. This repeat is of a cell containing No Additve during formation. Many more repeats can be shown upon request.

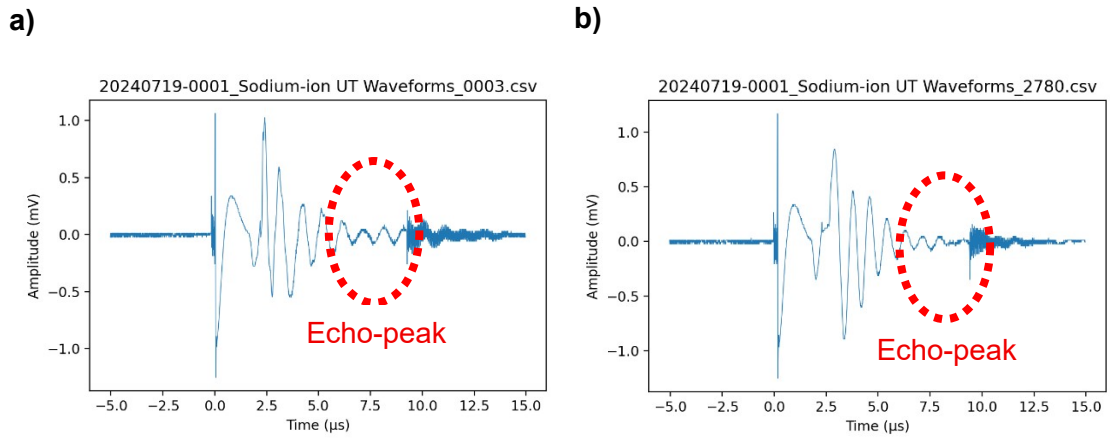

Figure S 16. Waveforms from the ultrasonic pulse tests, showing amplitude of the wave plotted against the Time of Flight of the ultrasonic signal, taken (a) at the start of the formation cycle and (b) at the end of the formation cycle

Ultrasonic Testing Results

Figure S *16* shows two ultrasonic waveforms, taken at the start of the formation cycle (**Figure S *16***a) and at the end (**Figure S *16***b). The waveform shape evolves over the course of the cycle, reflecting changes in the cell's internal structure, as ultrasonic pulses experience different levels of attenuation depending on the medium they pass through. In particular, signals traveling through regions of the cell where gas bubbles have formed are attenuated or scattered more strongly than those traveling through gas-free regions, due to the much larger acoustic impedance mismatch between the electrolyte/electrode and gas phases. The dashed oval in **Figure S *16*** highlights the time-of-flight (ToF) region of interest, which contains the first echo-peak generated after the signal has traversed the entire cell and reflected back. This echo is analysed because it provides information about the overall internal structure of the cell. The decrease in amplitude of the echo peak, highlighted by the red oval, from the beginning to the end of the formation cycle, indicates increased ultrasonic attenuation as gas evolves within the cell.

As has been widely described previously, ToF is inversely proportional to the speed the wave travels. The speed of the ultrasonic wave, c, through the cell is related to Young's modulus, E, and density, ρ (see Equations (1.0) and (1.1)):

$$c = \sqrt{\frac{E}{\rho}} \tag{1.0}$$

$$ToF = \frac{L}{c} = \frac{L}{\sqrt{\frac{E}{\rho}}} \tag{1.1}$$

ToF thus increases with the distance the signal travels, *L,* and with increasing density, and decreases with growing elastic moduli. The signal travels faster through a medium with greater elastic modulus. As the cell forms leading to gassing and changes to the elastic modulus and cell structure, the ToF increases. UT is therefore a vital tool for correlating to AE and determining gaseous reactions in the cells containing different electrolytes. Recent studies have investigated the effect of SoC of the electrode on the ToF of the signal in LIBs. [42,45,46] Future work will develop these studies in NIB

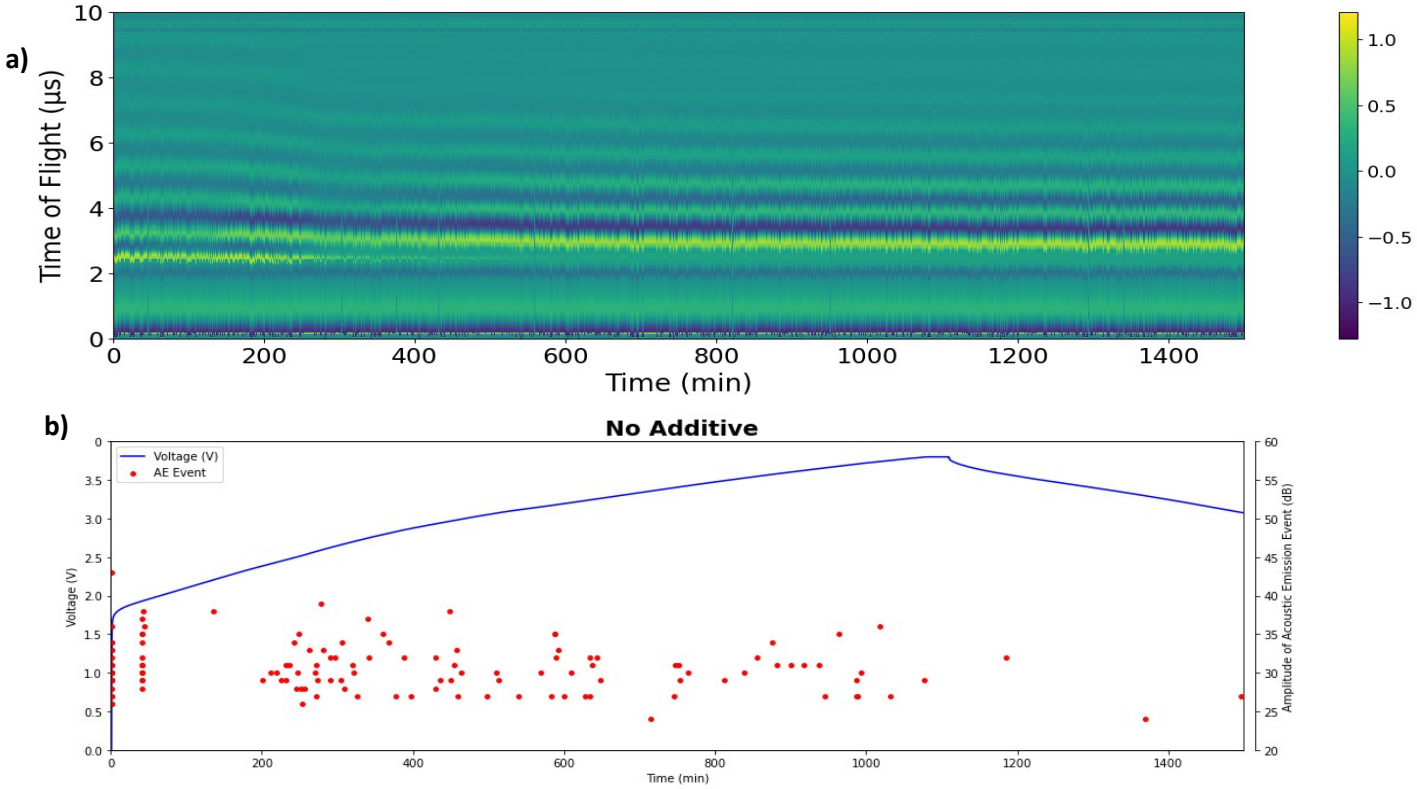

Figure S 17. Acoustic results from cells during f. (a) shows UT ToF plotted against time of experiment where amplitude of peaks in the UT pulses are represented by varying colours. (b) shows AE hit amplitude.

counterparts.

Figure S *17* (a) displays a colour map of the Ultrasonic Testing data, and the (b) plot represents the AE data for the formation cycle of a cell with no additives. Simultaneous UT was carried out which also show's signs of gassing during periods of AE activity. A UT ToF plot shows that peaks diminish in time-of-flight during charge, as seen by the thinning yellow streaks. ***(*Figure S *17 a)*** This result suggests that UT pulse signals were attenuated, likely caused by gas bubbles produced during formation. The UT result is supported by the appearance of AE hits around the same time (**Figure S *17*** (b)).

Machine Learning Waveform Analysis

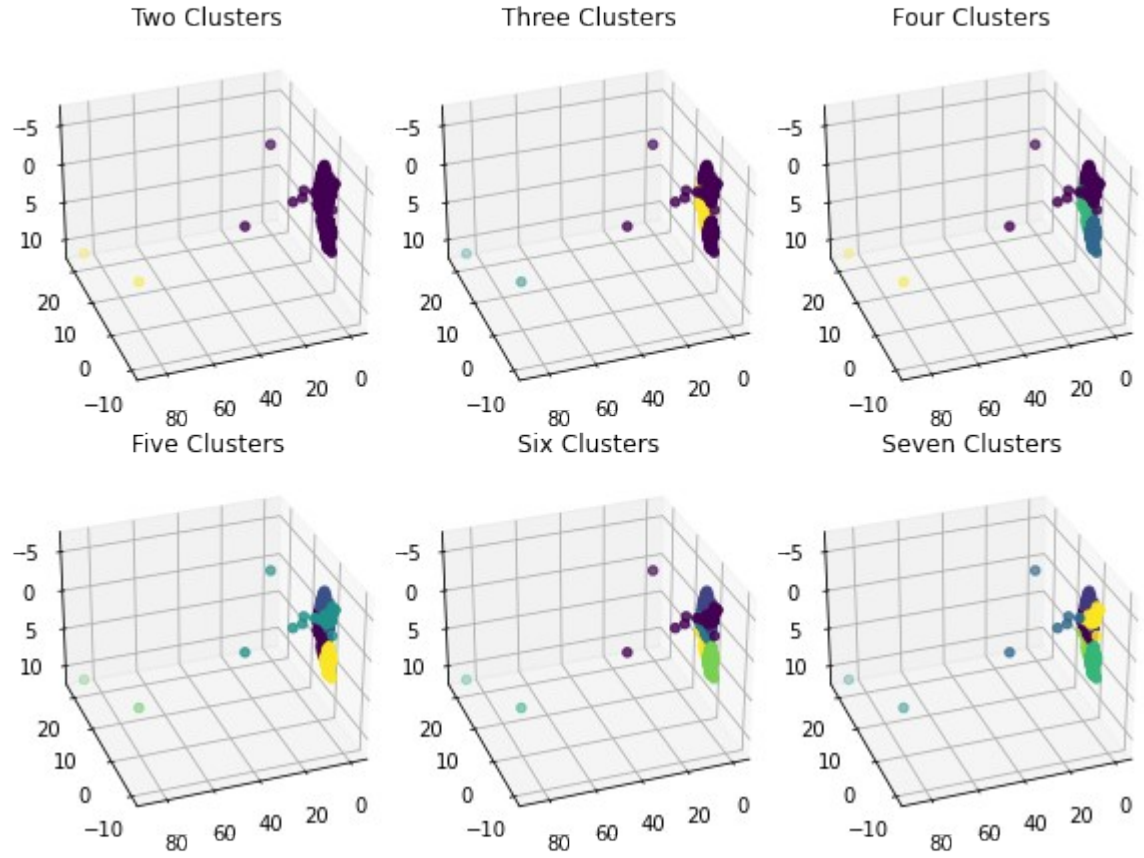

Figure S 18. Cluster analysis for unsupervised machine learning to determine types of waveforms.

The Acoustic waveforms analysed in this analysis are found in this public repository
https://doi.org/10.5522/04/30392215.v1

Electrochemistry

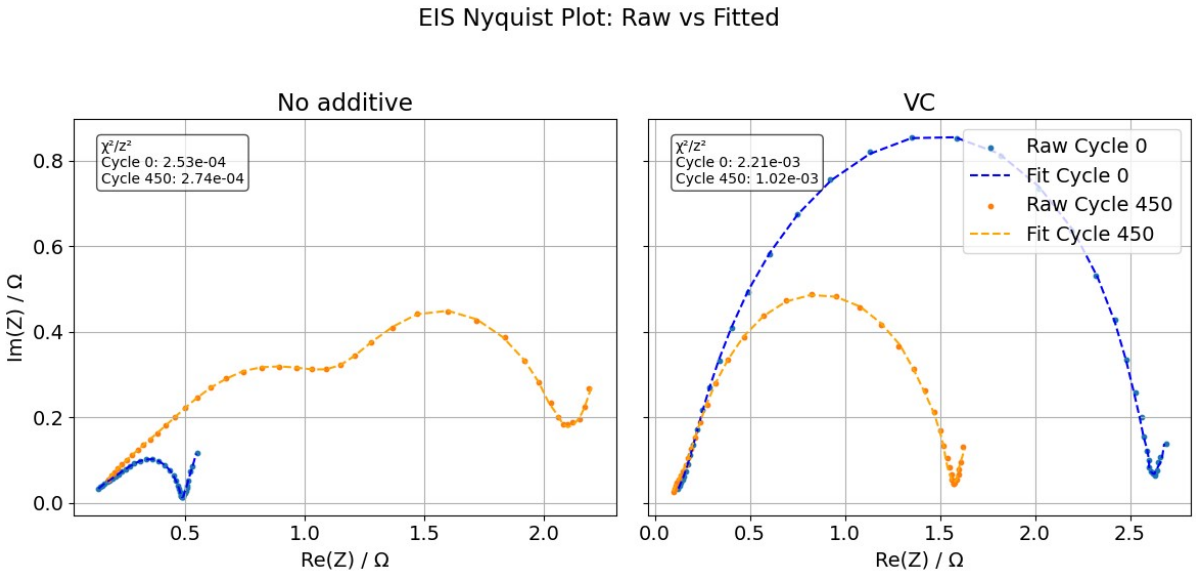

Figure S 19. Example of the high-quality Electrochemical Impedance Fitting. Examples show EIS fits for Cells containing No additive and VC additive after formation and after 450 cycles.

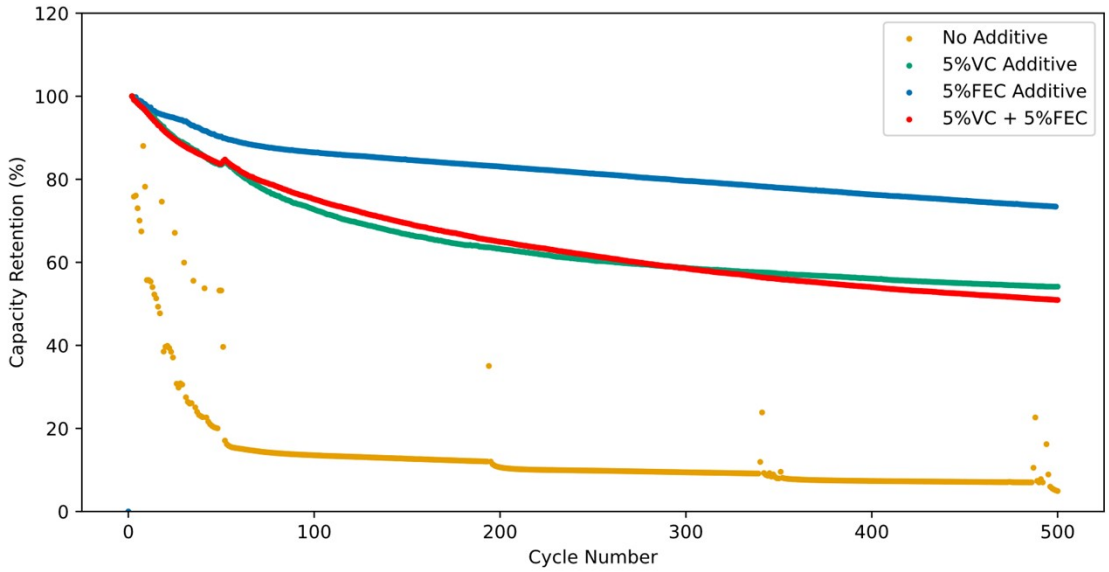

Figure S 20. EIS plots of the cell impedance after the formation cycle and then after 500 cycles. (e) Capacity retention for each electrolyte used. Cells were cycled at C/3 for 500 times between 1.5-3.8 V to understand the role of electrolyte in cell performance. These repeats were performed on the Novonix.

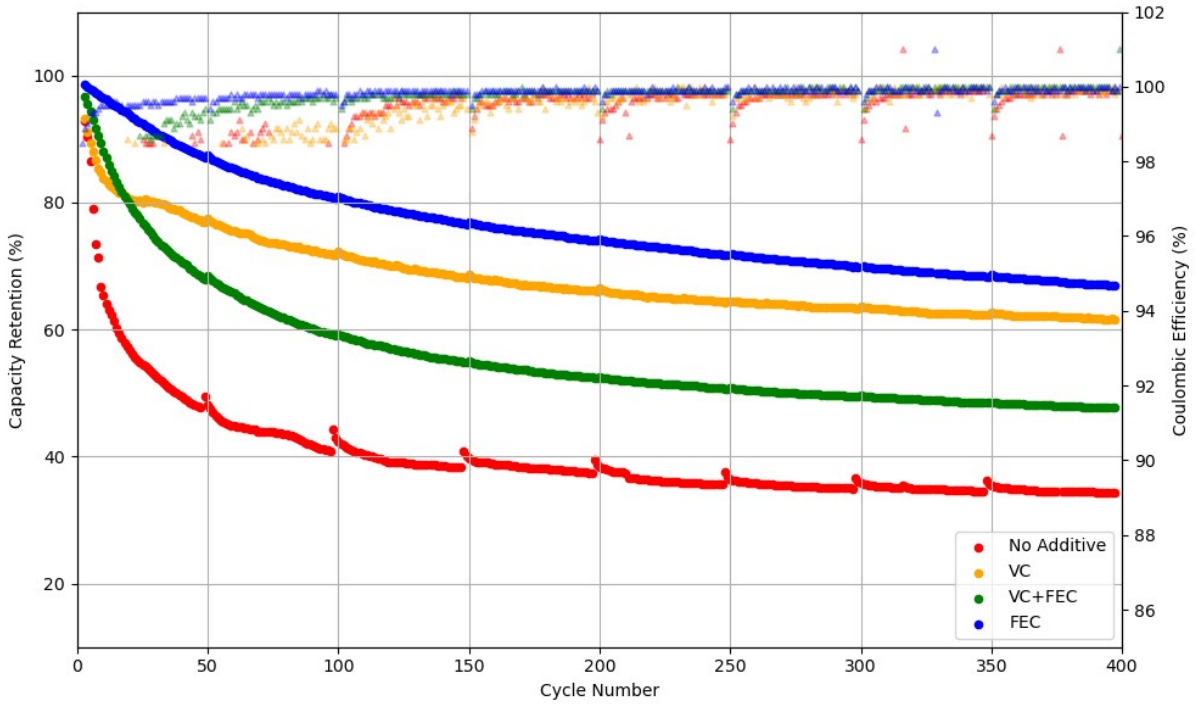

Figure S 21. Capacity retention and Coulombic Efficiency for each electrolyte used. Cells were cycled at C/3 for 500 times between 1.5-3.8 V to understand the role of electrolyte in cell performance. These repeats were performed on the Biologic Cyclers.

The repeated cycling data in **Figure S *21*** shows the capacity retention of the cells calculated as a percentage of the initial capacity of the cell, plotted against cycle number (repeats shown in SI). The results showed that the cell with no additive showed the poorest capacity retention, dropping significantly (20% capacity retention after 70 cycles) relative to the other chemistries. This poor performance of the cell containing no additive is likely due to the growth of a non-stable and poorly passivating SEI layer, which is also seen in the increased peak of the EIS in (a), indicative of a highly resistive SEI. The poor SEI will lead to continued gassing throughout cycling, leading to a greater separation of electrode layers and delamination, reducing the capacity further. In contrast, the cell with the FEC additive showed the best capacity retention, steadying and plateauing at just above 80%, suggesting that the use of FEC in SEI formation provided the best electrochemical behaviour of the cell, also shown with the EIS data. The cell with VC additive showed slightly better performance than the combination of VC + FEC additives, but their similar performance suggests that the presence of VC in the VC + FEC cell dictated the electrochemical behaviour of the cell. This result is consistent with the EIS data where the VC and VC + FEC Nyquist plots are similar, suggesting that it is the VC leading to the cells impedance and corresponding performance.

Longer-Term Acoustic Emission Testing

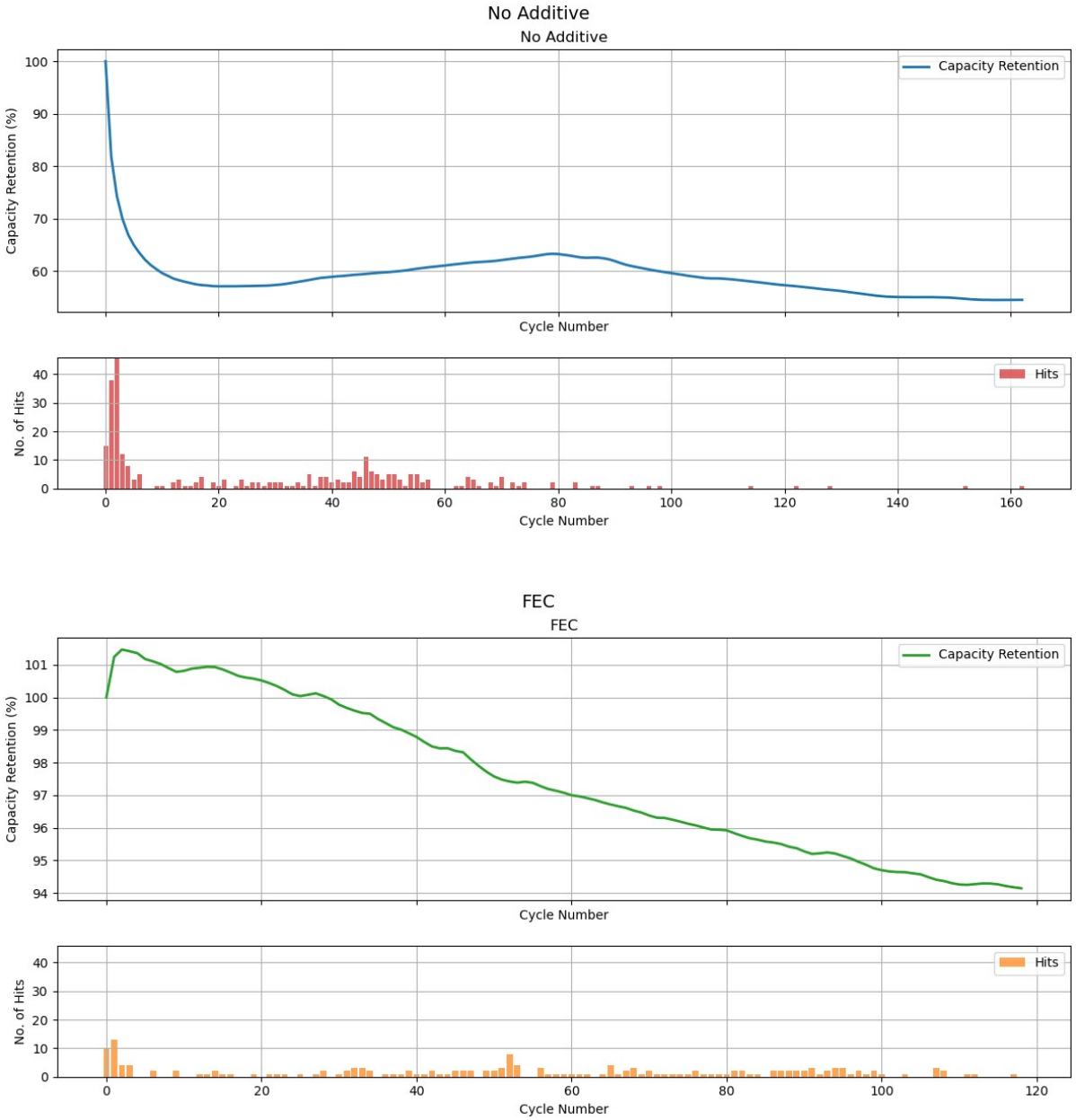

Figure S 22. Acoustic Emission results for Long Term Electrochemical testing for the cell containing 5% FEC and No additive. Results show the greater number of hits for the cell with no additive relative to 5% FEC.

X-Ray Computed Tomography

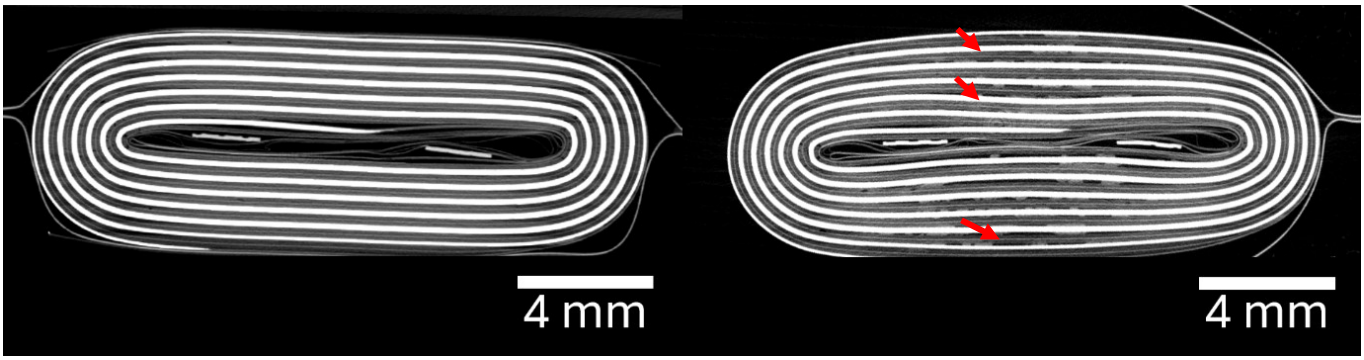

Figure S 23. X-ray Computed Tomography scans of the same cell containing no additive in its (a) pristine condition and (b) post-formation. The red arrows indicate gaps between layers likely caused by delamination due to gassing during formation indicated at the head of red arrows. Both (a) and (b) are an orthoslice at the same position/depth within the cell.

Alongside the gas analysis, X-ray Computed Tomography (CT) was also used at cell level to validate the origin of AE events within the cell. **Figure S23** displays how the X-ray CT of the cell with no additive can be used to illustrate gas evolution and ageing within the cell. **Figure S23** shows orthoslices from the 3D volume at the same location for both the pristine and post-formation of the SIB pouch cell. The pristine scan shows how the electrode layers are highly aligned in the 12 wound bindings around the central tabs (with the Cu negative electrode current collectors displaying the highest X-ray attenuation and appearing brightest in the image). After formation, gaps between the electrode layers and the separator were observed, as indicated by the red arrows. Analysis using 3D imaging software (Avizo) revealed that average electrode layer separation increased by ~22% (53,54), likely caused by gassing and particle volume expansion during formation. Similar X-ray CT results were observed in all cells containing additives post-formation, but the greatest layer separation occurred in the cell without additives. This observation aligns with previous findings, where the same cell exhibited the highest levels of gas generation and AE events.

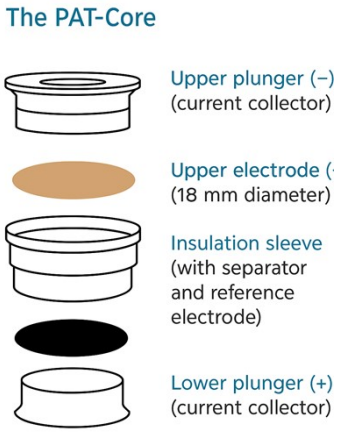

Figure S 24. Schematic Diagram of the PAT EL-Cell used for Three-electrode measurements.